

Effect of Flow and Steel Microstructure on the Formation of Iron Carbonate

Maria Di Bonaventura,^{†,***} Bruce Brown,^{*} Srdjan Nešić,^{*} and Marc Singer^{*}

Iron carbonate (FeCO_3) is a protective layer that can form on the surface of the steel as a by-product of CO_2 corrosion. This layer acts as a mass-transfer barrier and affects the rate of electrochemical reactions at the steel surface, thus slowing down further corrosion. Temperature, CO_2 partial pressure, and pH are the main environmental parameters controlling FeCO_3 properties. However, the combined effects of flow and material microstructure on the formation of FeCO_3 have not been well documented. In this research, two materials were used to determine the effect of microstructure on the formation of iron carbonate: an annealed low-alloy carbon steel (0.05 wt% C), formally API 5L X65, with ferrite and iron carbide (Fe_3C) precipitates microstructure, and UNS G10180 (0.18 wt% C), with either a ferritic–pearlitic or a tempered martensitic microstructure. FeCO_3 formation and retention of Fe_3C on the steel surface were investigated in experiments in a three-electrode glass cell under controlled water-chemistry conditions. Experiments were performed at two different flow rotational speeds and lasted 5 days. Scanning electrode microscopy, energy-dispersive x-ray spectroscopy, and x-ray diffraction analyses of specimen surface after exposure provided corrosion-product characterization. The experimental results clearly indicated the existence of a critical shear stress (although not universal and strictly dependent on experimental conditions) above which FeCO_3 could not nucleate and grow on the steel surface. In addition, the steel microstructure, rather, the carbon content, had a strong effect on the results with the ferritic–pearlitic steel clearly favoring FeCO_3 precipitation.

KEY WORDS: CO_2 corrosion, flow effects, microstructure, scaling, shear stress

INTRODUCTION

Iron carbonate (FeCO_3) is the most common corrosion product that can form on the surface of mild steel as a by-product of the CO_2 corrosion process. This precipitated FeCO_3 layer slows down further corrosion by acting as a diffusion barrier, preventing corrosive species from reaching the steel surface, and by directly affecting the kinetics of iron dissolution. On the other hand, iron carbide (Fe_3C), also known as cementite and classified as a “corrosion product,” is originally found in the material’s microstructure and, unlike FeCO_3 , does not precipitate on the steel surface. Rather, it represents the “left-over” portion of the steel structure, once the ferrite phase has been corroded away. The exposed porous Fe_3C network can act as a diffusion barrier for ferrous, hydronium, and carbonate ions creating local surface conditions favoring the formation of a FeCO_3 layer.

Ambiguous results have been found in the literature with regards to what microstructure favors FeCO_3 precipitation, and no consensus has been reached. Dugstad, et al., found that a ferritic–pearlitic microstructure did not favor FeCO_3 formation as corrosion rates remained high.¹ Ochoa, et al., found that both ferritic–pearlitic and quenched and tempered microstructures favored formation of a protective FeCO_3 layer.² However, these results were obtained at various environmental conditions and no direct comparison can be made between the research studies.

Farelas, et al.,³ studied the influence of an Fe_3C layer on the formation of FeCO_3 by using two different steel compositions and microstructures: API⁽¹⁾ 5L X65 tempered martensite and UNS G10180⁽²⁾ ferritic–pearlitic. Farelas concluded that formation of FeCO_3 is possible within the pores of the exposed “skeletal” Fe_3C layer, even when the bulk water-chemistry conditions are unfavorable for FeCO_3 precipitation. Although Farelas’s findings constituted a breakthrough in studying the role of Fe_3C , the author did not incorporate flow effects into his studies. Flow effects may play a major role in the formation of FeCO_3 within the pores of Fe_3C , because the Fe_3C layer is mechanically weak and thus susceptible to removal by flowing conditions.⁴ In a more recent study, leamsupapong, et al.,⁵ also found that the presence and characteristics of Fe_3C played a governing role in the formation of FeCO_3 on a UNS G10180 ferritic–pearlitic steel at intermediate pH values. His findings were similar to those of Farelas, in which Fe_3C acted as a diffusion barrier slowing diffusion of generated ferrous ions away from the surface. The higher concentration of ferrous ions near the metal surface increased FeCO_3 saturation value to initiate precipitation of FeCO_3 , whereas the bulk solution was as low as pH 5.4 and undersaturated with respect to FeCO_3 .⁵

Eliyan and Alfantazi, who found similar results to Farelas and leamsupapong, claimed that a ferritic–pearlitic microstructure was superior to other microstructures in regards to FeCO_3 formation as a result of the distribution of Fe_3C .⁶ On the

Submitted for publication: December 26, 2018. Revised and accepted: July 10, 2019. Preprint available online: July 10, 2019, <https://doi.org/10.5006/3118>.

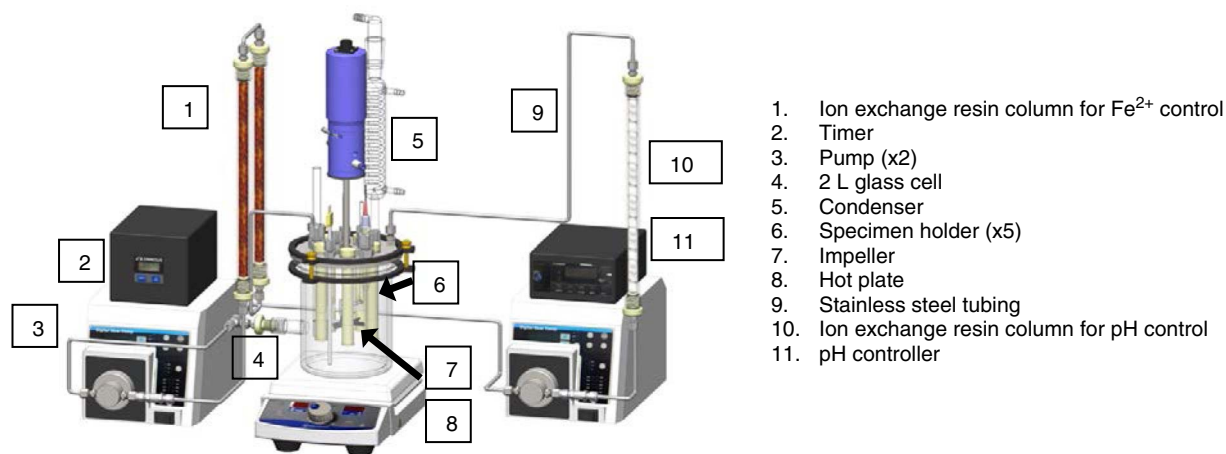
[†] Corresponding author. E-mail: maria.dibonaventura@bp.com.

^{*} Institute for Corrosion and Multiphase Technology, Department of Chemical and Biomolecular Engineering, Ohio University, Athens, Ohio 45701.

^{**} Current address: BP America, Houston, Texas 77079.

⁽¹⁾ American Petroleum Institute (API), 1220 L St. NW, Washington, DC 20005.

⁽²⁾ UNS numbers are listed in *Metals & Alloys in the Unified Numbering System*, published by the Society of Automotive Engineers (SAE International) and cosponsored by ASTM International.



1. Ion exchange resin column for Fe^{2+} control
2. Timer
3. Pump (x2)
4. 2 L glass cell
5. Condenser
6. Specimen holder (x5)
7. Impeller
8. Hot plate
9. Stainless steel tubing
10. Ion exchange resin column for pH control
11. pH controller

FIGURE 1. Three-electrode glass cell with stable solution chemistry and controlled mass-transfer setup (courtesy of Cody Shafer).

contrary, Berntsen stated that an exposed Fe_3C , obtained through precorrosion of the metal, did not have any beneficial impact in FeCO_3 formation.⁷ This was a result of the fact that FeCO_3 formed though most of the Fe_3C had spalled off during the experiments. Although Berntsen's study presented results at odds with what others found,³⁻⁵ the experimental conditions showed FeCO_3 saturation values in the range of 300–500. The very high concentration of ferrous ions in the bulk solution likely facilitated FeCO_3 formation rather than the material microstructure.

High flow velocities, which are common in various field applications, have been postulated either to lead to partial mechanical removal of FeCO_3 layers or to impede the nucleation and growth of FeCO_3 crystals on the steel surface. Previous studies have shown that partial removal of FeCO_3 can lead to an increase in metal loss and pitting—a very aggressive type of localized corrosion.⁸⁻⁹ Thus, it is imperative to understand how this corrosion product layer behaves and forms under a variety of environmental conditions, which can allow appropriate prediction of the corrosion rate. The overall objective of the current study is to identify if FeCO_3 formation is impeded by high flow velocities and if microstructural effects play a role.

EXPERIMENTAL PROCEDURES

The experimental system, shown in Figure 1, consists of a three-electrode electrochemical glass cell, 2 L in volume, that can accommodate an impeller in the center of the glass cell to achieve controlled flow conditions. The advantage of using an impeller with static specimens, instead of a more traditional rotating cylinder electrode (RCE) or rotating disc electrode (RDE), is that centrifugal forces, which are found on the RCE and RDE and can mechanically affect the formation of a corrosion-product layer, are eliminated. At the same time, multiple specimens can be used while making sure that each specimen is exposed to well-controlled and properly characterized mass-transfer and shear-stress conditions. In these experiments, five flat metal specimens, each with an exposed area of 1.6 cm^2 , were located at a fixed height and distance from the pitched blade turbine impeller. Out of the five specimens, three were used for surface and cross-sectional characterizations, one for electrochemical measurements, and one for weight loss (WL)

measurements (as outlined by procedure in ASTM G1-03).¹⁰ The water chemistry (pH and ferrous ion concentration) in these experiments was controlled by use of ion-exchange resin columns. The bulk pH of the solution was controlled with a pH meter/controller connected to a pump that would draw electrolyte out of the glass cell through a side port and flow it through an H ion-exchange resin column to maintain the bulk pH of the solution at $\text{pH } 6.6 \pm 0.03$. A second pump with a timer/controller would simultaneously flow solution through Na ion-exchange resin column to control the ferrous ion concentration in the solution. A timer was used to operate the second pump as there is no in situ technique to measure ferrous ion concentration in solution. Based on preliminary results, it was found that the ferrous ion concentration was best controlled when the pump was on for 20 min and off for 10 min. More details of the procedure for using ion-exchange resins to control water chemistry in electrochemical experiments has been explained in a previous publication by Zhong, et al.¹¹

Environmental conditions ($\text{pH } 6.6$, $T = 80^\circ\text{C}$) were selected to ensure optimal corrosion product layer-forming conditions in a 1 wt% NaCl electrolyte with initial FeCO_3 saturation value (S_{FeCO_3}) equal to 10. This saturation value ensured FeCO_3 layer formation. The desired initial ferrous ion concentration was obtained by adding 2 ppm Fe^{2+} into the bulk solution in the form of FeCl_2 . Deoxygenated aqueous FeCl_2 was prepared by dissolving ferrous chloride tetrahydrate ($\text{FeCl}_2 \cdot 4\text{H}_2\text{O}$) in deionized water sparged with nitrogen gas (N_2) for more than 30 min (oxygen-free solution). Aqueous ferrous ion concentrations were measured with FerroVer[†] iron reagent and a spectrophotometer at appropriate time intervals over the course of the experiments.

Each 5 day experiment was conducted at a constant flow velocity. Experiments were performed at two impeller speeds: 150 rpm and 250 rpm. For ease of comparison, equivalent liquid velocities in a hypothetical 10 in-diameter pipe were calculated. It is important to mention that these velocities are not just a simple unit conversion from rpm to m/s. Rather, this exercise was performed by calculating the mass-transfer coefficient of H^+ ions in the glass-cell setup and by determining the equivalent liquid velocity in a pipeline, by use of the established Sherwood correlation,¹² which would generate the same mass-transfer conditions.¹²⁻¹³ It is understood that by doing so, the mass-transfer characteristics are matched but not the shear stress. Wall shear stresses on the steel specimen

[†] Trade Name.

Table 1. Test Matrix Showing Experimental Parameters Used to Study the Effect of Microstructure and Flow on FeCO₃ Formation

Parameters	Conditions
Experimental Setup	2 L glass cell
Materials (microstructure)	UNS G10180 (ferrite-pearlite), UNS G10180 (tempered martensite), API 5L X65 (ferrite with Fe ₃ C precipitates)
Electrolyte	1 wt% NaCl
Total Pressure	1 bar (10 ⁵ Pa)
Temperature	80°C
CO ₂ Partial Pressure	0.53 bar (5.3 × 10 ⁴ Pa)
pH	6.6±0.03
[Fe ²⁺]	1 ppm–6 ppm
Saturation w.r.t. FeCO ₃	10–30
Impeller Rotational Speeds	150 rpm and 250 rpm
Equivalent Pipeline Velocity in 10 in pipe	0.4 m/s (150 rpm) and 0.6 m/s (250 rpm)
Shear Stress	0.3 Pa (150 rpm) and 0.5 Pa (250 rpm)
Surface Analysis	scanning electrode microscopy (SEM), x-ray diffraction (XRD), and cross section
Corrosion Measurement Methods	LPR, electrochemical impedance spectroscopy (EIS), and WL

Table 2. Chemical Composition of API 5L X65 (wt%)

API 5L X65 Mild Steel (Balance Fe)						
C	Mn	Nb	P	S	Ti	V
0.05	1.51	0.03	0.004	<0.001	0.01	0.04

Table 3. Chemical Composition of UNS G10180 (wt%)

UNS G10180 (balance Fe)									
Al	As	C	Co	Cr	Cu	Mn	Mo	Nb	Ni
0.008	0.006	0.18	0.003	0.12	0.18	0.75	0.020	0.002	0.065
P	S	Sb	Si	Sn	Ti	V	W	Zn	Zr
0.011	0.021	0.009	0.16	0.009	0.002	0.003	0.014	0.004	0.003

surface were calculated via computational fluid-dynamics simulations;^{13–14} both are reported in Table 1. The duration of the experiments was 5 d, enabling sufficient time for Fe₃C to form, as indicated in previous experiments of this kind.^{3,5} In order to show reproducibility of results, experiments at the highest velocity were repeated.

2.1 | Materials

Three different materials and/or microstructures were tested: an annealed low-alloy carbon steel (originally API 5L X65) with ferritic microstructure and Fe₃C precipitates (0.05 wt% C), a ferritic-pearlitic UNS G10180, and a tempered martensitic UNS G10180. Tables 2 and 3 show material compositions for the API 5L X65 and UNS G10180 specimens, respectively.

The UNS G10180 material was chosen to provide test specimens with the same composition, but two different microstructures. As received, the material has a ferritic-pearlitic microstructure as shown in Figure 2(a). The pearlite consists of thin Fe₃C lamellae and ferrite. A tempered martensitic microstructure was obtained by heating to 950°C, holding

for 45 min, and quenching in water for 5 min, followed by tempering at 500°C for 2 h. The thermal treatment was determined based on the time-temperature transformation diagrams, equivalent carbon content, and desired final microstructure.^{14–18} Figure 2(b) shows the microstructure of the UNS G10180 material after thermal treatment. It can be verified that the microstructure obtained was consistent with tempered martensite.^{14–18} The hardness of the tempered martensite UNS G10180 was 97±2.2 (Rockwell B, 100 kg load), which is consistent with literature values for same material and thermal treatment yielding a martensitic microstructure.¹⁹

The API 5L X65 material was chosen to develop a test specimen with a similar microstructure but different composition from the UNS G10180. API 5L X65 specimens underwent a thermal treatment (heated at 930°C for 3 h)^{14–18} to match the grain size to that of UNS G10180. It is understood that the yield strength after a thermal treatment no longer matches the definition of an API 5L X65. Figure 2(c) shows the microstructure of the “annealed API 5L X65” tested, which shows dispersed cementite particles. These cementite particles are difficult to see

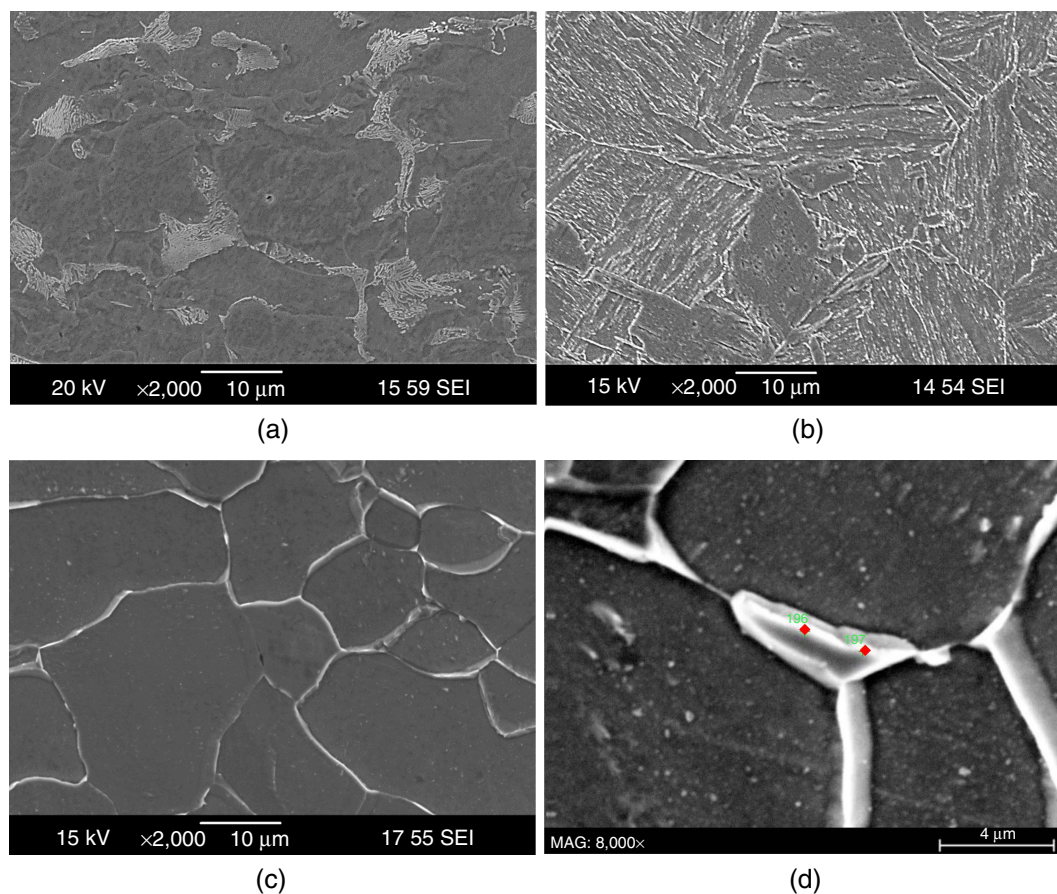


FIGURE 2. SEM image of (a) as-received UNS G10180 showing a ferritic-pearlitic microstructure, (b) UNS G10180 after thermal treatment showing a tempered martensitic microstructure, (c) API 5L X65 low-carbon steel after annealing process showing a ferritic microstructure with cementite precipitates, and (d) API 5L X65 low-carbon steel after annealing process showing a ferritic microstructure with cementite precipitates used for energy-dispersive x-ray spectroscopy (EDS) analysis.

as a result of the low carbon content of the material (0.05 wt% C); Figure 2(d) shows an image used for energy-dispersive x-ray spectroscopy (EDS) analysis performed on the two areas highlighted in red. The EDS analysis performed was consistent with these precipitates being Fe_3C based on the iron to carbon ratio, with no presence of alloying elements (94.8 at% Fe, and 5.18 at% C). The microstructure is consistent with that of a ferritic microstructure with cementite precipitated at the grain boundaries. Other researchers have used EDS analysis to detect Fe_3C and FeCO_3 in similar conditions,^{3,20} which were further confirmed via electrochemical testing. It is also noted that the equilibrium weight fractions of Fe_3C and pearlite, calculated using the lever rule for this material, are 0.44% and 4.1%, respectively. In these conditions, the formation of the pearlite microconstituent is not likely.

2.2 | Specimen Preparation

Steel specimens for WL and electrochemical measurements all had dimensions of 1.27 cm × 1.27 cm × 0.2 cm. Specimens were wet polished with silicon carbide abrasive paper up to 600 grit in order to ensure uniform surface preparation prior to the start of experiments; this included rinsing with isopropyl alcohol and using ultrasonication to remove any residue from the specimen surfaces. Specimens were dried with cold air before being mounted into a specimen holder. For the specimen used for electrochemical measurements, an insulated wire was soldered to its back prior to placement in an

epoxy mold, which was connected to a potentiostat. The mold was filled with an epoxy mixture to avoid any liquid penetration that could cause galvanic corrosion.

2.3 | Electrochemical Measurements

A Gamry[†] potentiostat was used for electrochemical and potential measurements. The working electrode was polarized from -5 mV to +5 mV vs. the open-circuit potential, with a scan rate of 0.125 mV/s for linear polarization resistance (LPR) measurements. The B value that was used was 26 mV/decade,^{3,5,21-22} obtained from the literature as being typical for low-temperature CO_2 corrosion of mild steel. The polarization resistance from LPR measurements was used to calculate the current density (i_{corr} , A/cm²) and, in turn, the corrosion rate in millimeters per year (mm/y) by use of the Stern-Geary Equation^{1,3,23-24} as follows:

$$\text{Corrosion rate} \left(\frac{\text{mm}}{\text{y}} \right) = \frac{a i_{\text{corr}} \text{MW}}{\rho n F}, \quad (1)$$

where MW is the molecular weight of iron (g/mol), ρ is the density of iron (g/cm³), n is the number of electrons involved in the electrochemical reaction, F is Faraday's constant, and a is a conversion factor to obtain corrosion rate in mm/y units.

EIS measurements at high frequencies were also collected in order to obtain a solution resistance and correct the

polarization resistance obtained from LPR measurements. There are uncertainties associated with the choice of scan rate and B values, especially as the surface state and chemistry of the corrosion specimen are changing over the course of the experiment. Consequently, WL measurements were also obtained for this work. LPR is used to obtain trends whereas WL measurements can give a better indication of corrosion rates.

2.4 | Specimen Characterization

Steel specimens were removed on the 1st, 3rd, and last day for surface characterization to determine nature of corrosion product present (if any). A JEOL 6390LV[†] SEM was used to characterize the surface morphology of all specimens. After completion of surface characterization, specimens were mounted in epoxy and prepared for cross-sectional analysis by SEM; this permitted characterization of layer morphology, thickness, and surface topography, as well as any formation of FeCO_3 within the Fe_3C network. The EDS coupled to the SEM was also used for elemental analysis. Some of the remaining

specimens removed on the 5th day were analyzed by XRD (Rigaku Ultima IV[†] with Cu K α radiation from 10 to 70 2 θ) to characterize compounds formed on the steel surface and others were used to determine WL corrosion rates. All experimental parameters are summarized in Table 1.

RESULTS AND DISCUSSION

3.1 | UNS G10180 Ferritic–Pearlitic Steel

3.1.1 | Water Chemistry

Solution pH and ferrous ion concentration were controlled well during the course of the experiments. The pH was controlled within a ± 0.03 deviation from the desired value of pH 6.60 for both rotational speeds. The Fe^{2+} concentration was also controlled by use of the ion-exchange resin within the range of 1 ppm to 6 ppm, with the desired value being 2 ppm ($\text{S}(\text{FeCO}_3) \approx 10$). There was a slight increase of ferrous ion concentration for the 250 rpm experiment, but the average was maintained at a value of 3.5 ppm, which was still within the desired range.

3.1.2 | Corrosion Rates

Figure 3 shows the comparison of LPR corrosion rate over time for the two rotational speeds. It can be observed that initial corrosion rates start at about 2 mm/y and increase over time, mainly because of the buildup of Fe_3C . Although this increase of corrosion rate resulting from buildup of Fe_3C , as detected by LPR, is real, the actual magnitude of the increase of the corrosion rate may be exaggerated 2–3 times when using this technique (this can be readily deduced by comparing the time-averaged LPR and WL corrosion rates). This is because the LPR measurements cannot account for the changing surface area for the cathodic reaction. Steels that contain the Fe_3C phase corrode at faster rates than pure iron as Fe_3C acts as an active cathodic site.^{4,6,17,25} In other words, the presence of Fe_3C increases the overall cathodic area, which in turn promotes the dissolution of the iron.^{4,6,7,17,25} This increase in corrosion rate over time has been termed as the “active corrosion stage.”^{3,5} For the 150 rpm experiment, the corrosion rate stopped

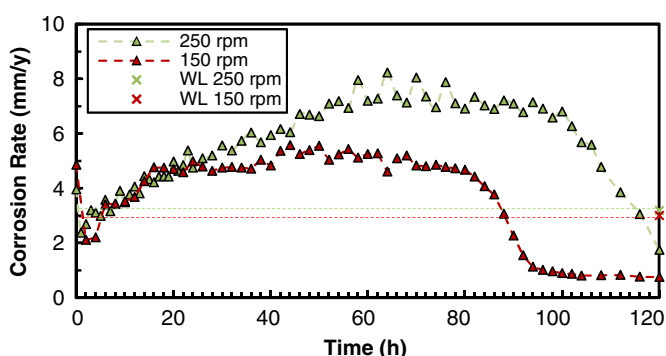


FIGURE 3. Comparison of LPR corrosion rate over time and WL measurements for 150 rpm ($V_{eq} = 0.4$ m/s, 0.3 Pa) and 250 rpm ($V_{eq} = 0.6$ m/s, 0.5 Pa) and WL corrosion rates; experiments with UNS G10180 ferritic–pearlitic microstructure steel.

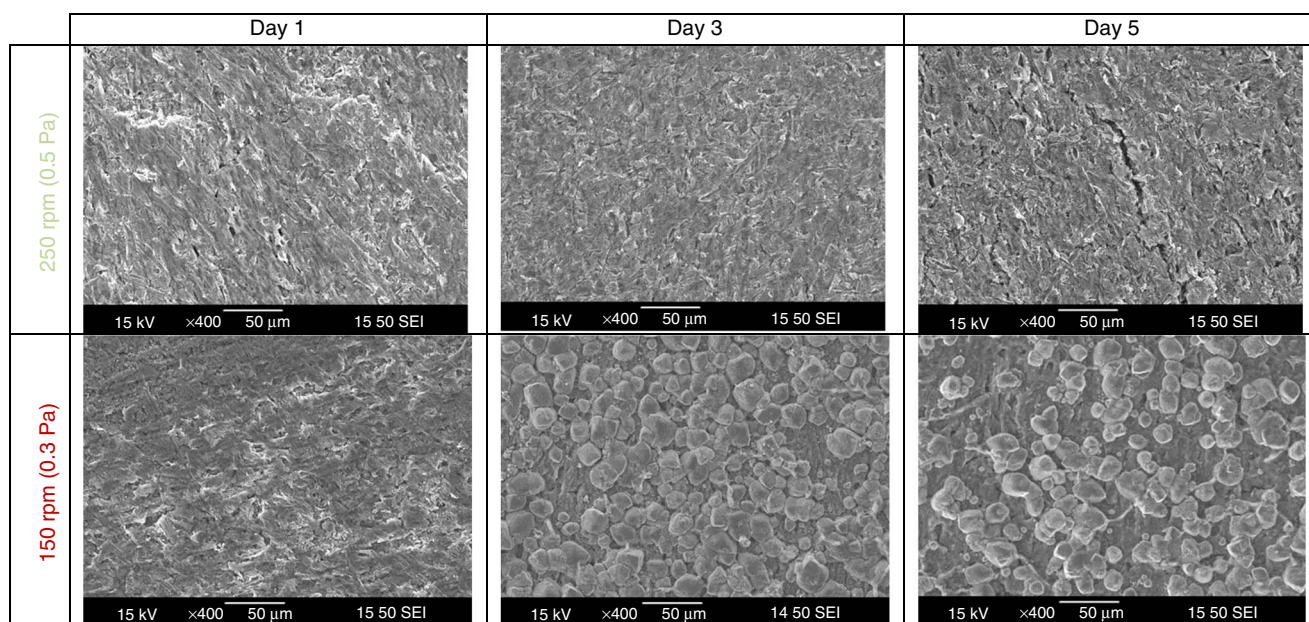


FIGURE 4. Comparison of surface morphologies over time for 150 rpm ($V_{eq} = 0.4$ m/s, 0.3 Pa) and 250 rpm ($V_{eq} = 0.6$ m/s, 0.5 Pa) experiments with UNS G10180 ferritic–pearlitic microstructure steel.

increasing after the 1st day and maintained a stable value until 65 h, when it decreased, reaching a low and steady value indicative of FeCO_3 formation. The stage at which the corrosion rate is at a low and steady value has been referred to as the "pseudo-passivation" stage.^{3,5} For the 250 rpm experiment, the corrosion rate increased for the first 80 h. After that, the corrosion rate rapidly decreased, which was also indicative of FeCO_3 formation. The stage at which the corrosion rate started to decrease but had not yet reached a stable value is known as the "nucleation and growth of FeCO_3 " stage.^{3,5} Repeats were not performed for UNS G10180 ferritic-pearlitic as the results matched the literature for this specific material and microstructure.^{3,5}

3.1.3 | Surface Morphologies and Characterization

Figure 4 shows various SEM images of the surface of the specimens removed on the 1st, 3rd, and 5th day of the experiments for rotational speeds of 250 rpm and 150 rpm. The

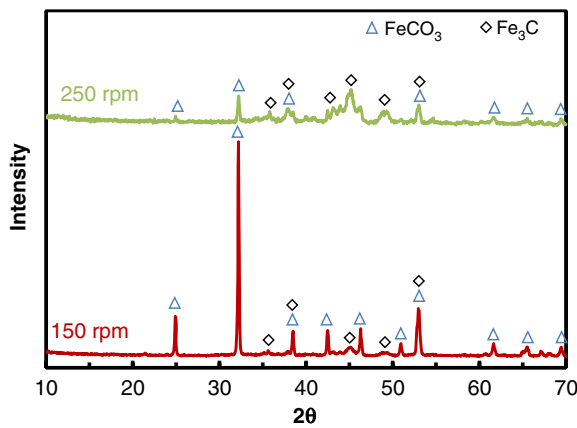


FIGURE 5. XRD analysis on UNS G10180 ferritic-pearlitic specimens for 150 rpm ($V_{eq} = 0.4$ m/s, 0.3 Pa) and 250 rpm ($V_{eq} = 0.6$ m/s, 0.5 Pa) experiments.

surface morphology of the 1st-day specimen for both rotational speeds show similarities: a rough surface with no visible precipitation of FeCO_3 . However, differences are found on specimens removed on the 3rd day as there is visible precipitation of FeCO_3 , in the form of prismatic crystals, for the 150 rpm experiment, whereas the 250 rpm experiment still shows a bare rough steel surface with no precipitation. For the 5th day of the experiment, the surface of the specimen for the 250 rpm experiment shows some grooves on the surface and no precipitation of FeCO_3 . However, grooves have been associated with a thick and porous layer of Fe_3C , as the ferrite phase preferentially corrodes, leaving cementite behind.^{3,26} The specimen for the 150 rpm experiment taken out on the 5th day shows a surface covered by FeCO_3 prismatic crystals, which are protective as indicated by the decrease of corrosion rate to a low and steady value as shown in Figure 3. Figure 5 shows the XRD patterns for the specimens retrieved from the 150 rpm and 250 rpm experiments after day 5. The dominant corrosion product for the 150 rpm experiment was FeCO_3 . For the 250 rpm experiments, the corrosion products were Fe_3C and FeCO_3 . The XRD analysis confirmed the formation of FeCO_3 on both specimens. However, as shown by the surface morphologies and the XRD patterns (Figures 4 and 5, respectively) FeCO_3 was more dominant on the 150 rpm specimen, which confirmed that there was an effect of flow on the formation of FeCO_3 . It is also noteworthy that the corrosion product layers are sufficiently thick that no diffraction from substrate ferrite ($\alpha\text{-Fe}$) was observed.

3.1.4 | Cross-Sectional Morphologies

Figure 6 shows cross-sectional morphologies for both rotational speeds for the extracted specimens after days 1, 3, and 5. For the 1st day, it can be seen that no significant corrosion had occurred and that Fe_3C is only about 5 μm thick for both experiments. For the 3rd day, a more significant Fe_3C network developed in both experiments. For the 150 rpm experiment after day 3, it can be observed that some FeCO_3 had precipitated within the porous layer of Fe_3C , but it did not cover

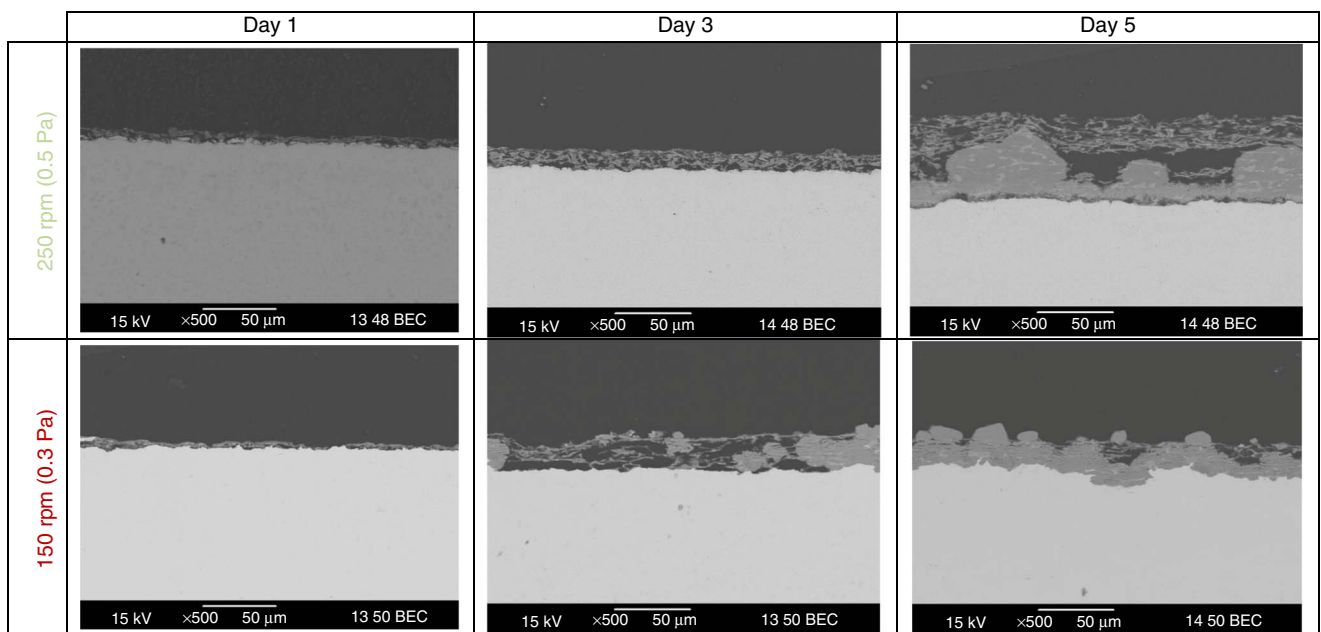


FIGURE 6. Comparison of cross-sectional morphologies over time for 150 rpm ($V_{eq} = 0.4$ m/s, 0.3 Pa) and 250 rpm ($V_{eq} = 0.6$ m/s, 0.5 Pa) experiments with UNS G10180 ferritic-pearlitic microstructure steel.

the steel surface fully, which was why the corrosion rate had not significantly decreased during this time, as shown in Figure 3. Finally, on day 5, the 150 rpm specimen shows that FeCO_3 had precipitated fully within the porous layer of Fe_3C . The 250 rpm specimen also shows that some precipitation occurred within the pores of Fe_3C but only close to the surface of the steel, which was why FeCO_3 prismatic crystals were not visible on the surface of the specimen, as shown in Figure 4.

3.2 | UNS G10180 Tempered Martensitic Steel

3.2.1 | Water Chemistry

The pH was controlled within a ± 0.03 range from the initial pH value of 6.60. The average pH value for both experiments was 6.59. Even though a maximum of 7.7 ppm Fe^{2+} was obtained during the 250 rpm experiment, the average value of all data obtained was 4.0 ppm Fe^{2+} (saturation $S(\text{FeCO}_3) \approx 25$). No significant changes in pH and ferrous ion concentration were observed; thus, it can be concluded that environmental conditions were well controlled during the experiments.

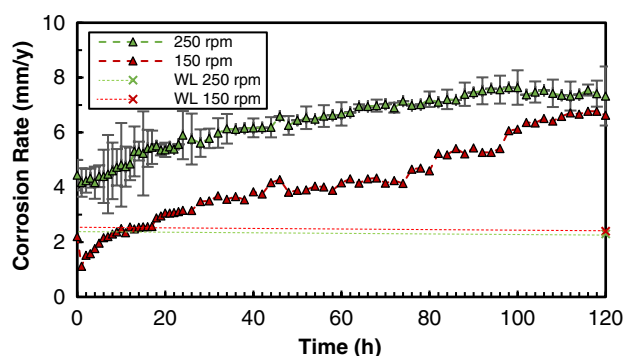


FIGURE 7. Comparison of LPR corrosion rate over time for 150 rpm ($V_{eq} = 0.4$ m/s, 0.3 Pa) and 250 rpm ($V_{eq} = 0.6$ m/s, 0.5 Pa) and WL corrosion rates; experiments with UNS G10180 tempered martensite microstructure steel.

3.2.2 | Corrosion Rates

Figure 7 shows the corrosion-rate measurements obtained over time. It can be seen, similar to the case of UNS G10180 ferritic–pearlitic steel, that LPR corrosion rates increased over time. Once again, this was the result of the preferential corrosion of the ferrite phase, leaving the Fe_3C behind, which acted as a cathode.^{4,6,17,25} However, unlike the UNS G10180 ferritic–pearlitic steel as shown in Figure 3 and previous studies,^{3,5} UNS G10180 tempered martensitic steel showed only an active corrosion stage. This trend may be an indication that formation of FeCO_3 did not occur, as a low and steady corrosion rate was never achieved. Lastly, the corrosion rate obtained through WL measurements did not match the corrosion rate obtained through electrochemical measurements, similar to the findings in UNS G10180 ferritic–pearlitic steel, because the presence of Fe_3C accelerated electrochemical corrosion rates in a way that is not accurately measured by LPR.

3.2.3 | Surface Morphologies and Characterization

Figure 8 shows SEM images of the surface of the specimen for 250 rpm and 150 rpm experiments removed at various time intervals. The surface morphology of all specimens removed on the 1st day show a “wrinkled” surface with more defined grooves on the 250 rpm specimen than on the 150 rpm specimen. Grooves became more defined, changing their appearance to that of cracks through the course of the experiments for both rotational speeds. Although the same trend was followed in both experiments, it can be observed that the 250 rpm condition shows wider cracks than those from the 150 rpm experiment. As for the case of UNS G10180 ferritic–pearlitic steel, cracks are related to exposure of a Fe_3C network.^{3,26} Other researchers have suggested that these cracks, visible to the naked eye, appear during the drying process as water is removed from the Fe_3C corrosion-product layer.^{27–29} There was no evidence of FeCO_3 formation, as there was no presence of prismatic-shaped crystals on the steel surface.

Figure 9 shows XRD analysis done on specimens removed on the last day. Both 250 rpm and 150 rpm specimens

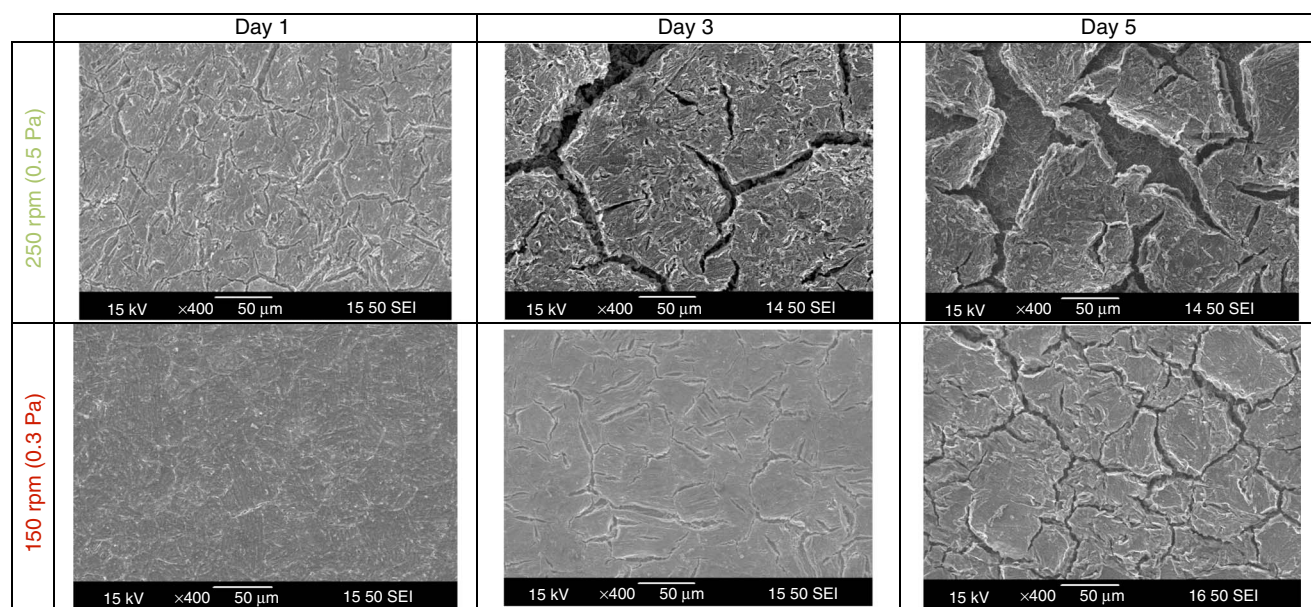


FIGURE 8. Comparison of surface morphologies over time for 150 rpm ($V_{eq} = 0.4$ m/s, 0.3 Pa) and 250 rpm ($V_{eq} = 0.6$ m/s, 0.5 Pa) experiments with UNS G10180 tempered martensite microstructure steel.

show the presence of Fe_3C and iron and an absence of FeCO_3 . Nonetheless, the Fe_3C peaks for the 250 rpm specimen are less pronounced than those from the 150 rpm XRD pattern. On the contrary, the substrate ferrite ($\alpha\text{-Fe}$) peaks are more pronounced for the 250 rpm specimen than for the 150 rpm specimen. This may be a result of the thickness and compactness of the Fe_3C .

3.2.4 | Cross-Sectional Morphologies

Figure 10 shows the cross-sectional morphologies of specimens in Figure 8. After the 1st day, there was no presence of corrosion product on the steel surface; no significant corrosion had occurred at this time. The cross sections from the 5th day show some exposed Fe_3C on the surface of the specimen, but no presence of FeCO_3 within the pores of the Fe_3C . This could be attributed to the distribution of the cementite in the material microstructure as the distribution of Fe_3C

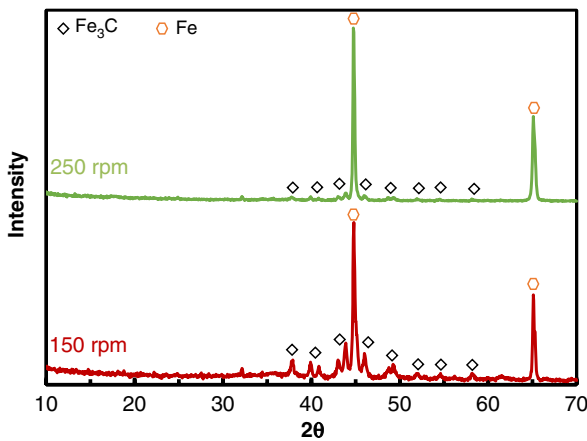


FIGURE 9. XRD analysis on UNS G10180 tempered martensitic specimens for 150 rpm ($V_{eq} = 0.4$ m/s, 0.3 Pa) and 250 rpm ($V_{eq} = 0.6$ m/s, 0.5 Pa).

was unordered and discrete in the material microstructure; Fe_3C was more subjected to removal by flow ("weaker" Fe_3C layer), which allowed for release of ferrous ions into the electrolyte as opposed to what was found in the ferritic-pearlitic microstructure of material with the same composition.

3.3 | API 5L X65 Annealed Steel

3.3.1 | Water Chemistry

As has been the case for all materials and rotational speeds tested so far, pH values and ferrous ion concentration were well-controlled and stable for all experiments throughout their entire duration.

3.3.2 | Corrosion Rates

Figure 11 shows corrosion rate over time for both the 150 rpm and 250 rpm experiments. It can be seen that corrosion rates stay stable over time and did not increase, which follows a similar trend to reported corrosion rates of pure iron.²⁵ This may be associated with the fact that the carbon content of this material is low (0.05 wt%) and the Fe_3C exposed was weak enough to be sheared away by flow and thus did not affect the corrosion rate. Previously, it had been reported that the carbon content did affect corrosion rate of steels.^{7,30-31} Additionally, the distribution of Fe_3C also affects the corrosion-rate behavior;⁶ however, a study performed by Al-Hassan, et al., concluded that there is no true effect of microstructure at temperatures above 60°C on corrosion rates,³² which contradicts these findings, as shown in Figures 3, 7, and 11. Clearly, the findings show different corrosion-rate behavior depending on the microstructure and carbon content, which correlates with previous studies.^{3,5,33}

3.3.3 | Surface Morphologies and Characterization

Figure 12 shows the changes of surface morphology during the course of the experiment. No major differences were observed on the surface of the specimens removed after the 1st day; both specimens show a rough surface. Nevertheless,

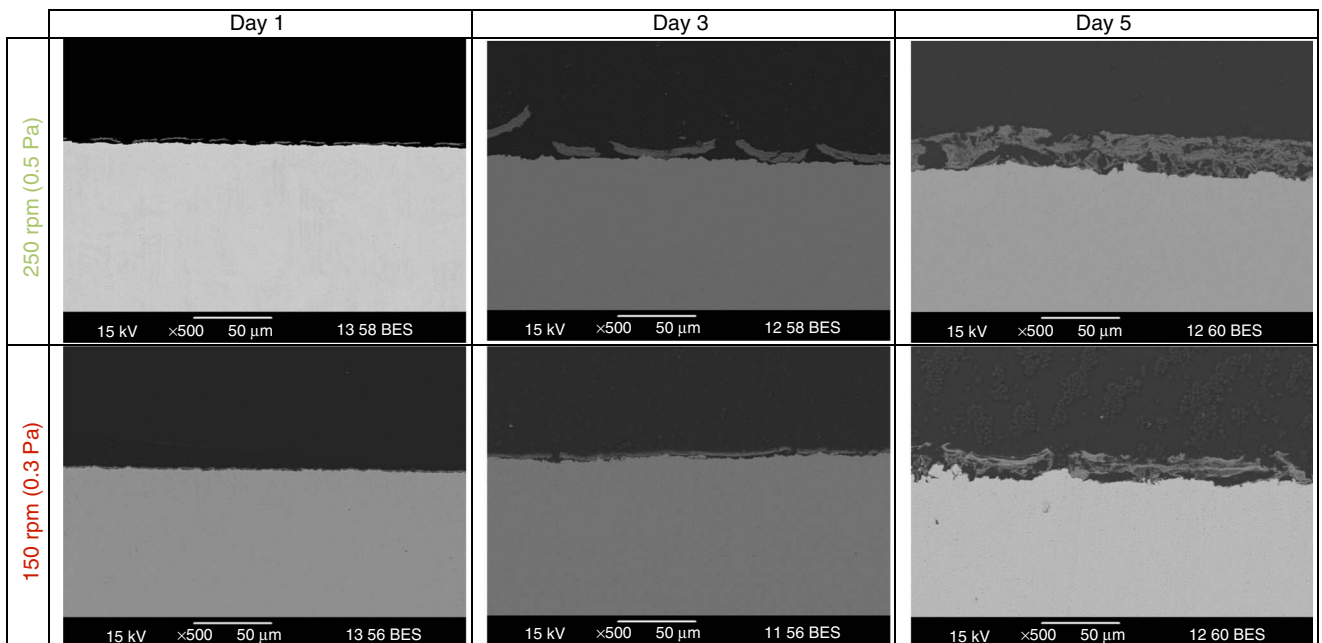


FIGURE 10. Comparison of cross-sectional morphologies over time for 150 rpm ($V_{eq} = 0.4$ m/s, 0.3 Pa) and 250 rpm ($V_{eq} = 0.6$ m/s, 0.5 Pa) experiments with UNS G10180 tempered martensite microstructure steel.

some differences are noted as grooves, which are more noticeable on the specimen retrieved from the 250 rpm experiment than from the 150 rpm experiment on the 5th day. These cracks have the same morphology as seen in previous studies, where they have been associated with Fe_3C presence.^{3,26} FeCO_3 is absent as there are no precipitated crystals on the surface of the specimens. The entire surface was evenly corroded and no indication of localized corrosion could be found.

Figure 13 shows the XRD patterns for the surface of the specimen taken out on the 5th day of the experiment. It can be seen that only pure iron ($\alpha\text{-Fe}$) peaks are present, and no corrosion products, such as FeCO_3 and Fe_3C , were identified, indicating that Fe_3C either was never present or was removed by flow, which may be a result of either the low carbon content^{7,30-31} or the distribution of Fe_3C .³²

3.3.4 | Cross-Sectional Morphologies

Figure 14 shows cross-sectional morphologies of the specimens shown in Figure 12. There was no significant evidence of Fe_3C up to the first 3 d of corrosion. On the 5th day, however, a thin layer appeared on the steel surface. This was

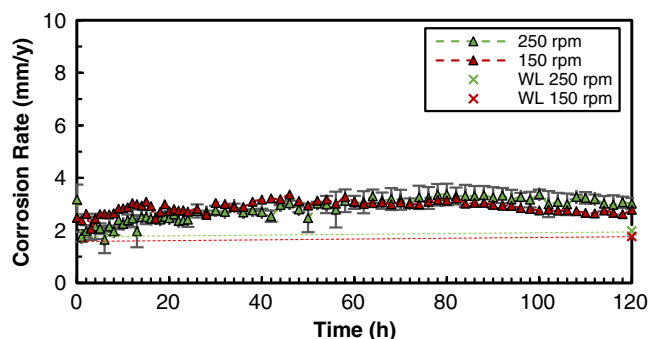


FIGURE 11. Comparison of LPR corrosion rate over time for 150 rpm ($V_{eq} = 0.4$ m/s, 0.3 Pa) and 250 rpm ($V_{eq} = 0.6$ m/s, 0.5 Pa) and WL corrosion rates; experiments with annealed API 5L X65.

confirmed by EDS to be a thin layer of Fe_3C and alloying elements, as shown in Figure 15. This correlated with the surface morphologies obtained by SEM, but not with XRD analysis. As shown in Figure 13, the Fe_3C was very thin and could not be detected by XRD as a result of the penetration depth by incident x-rays governing the magnitude of the detected diffraction peaks.

ANALYSIS

Steel microstructure, along with carbon content, played a key role in precipitation of FeCO_3 . It was found that a ferritic-pearlitic microstructure with a 0.18 wt% C favored precipitation of FeCO_3 within the Fe_3C network. Accordingly, the results indicate that the order and distribution of Fe_3C were crucial in regard to FeCO_3 precipitation. The lamellar structure of Fe_3C in tight microconstituents (pearlite) allowed for favorable local conditions for FeCO_3 precipitation from “trapped” ferrous ions,

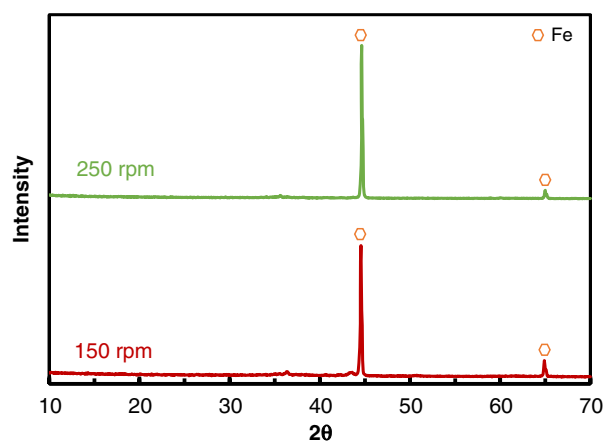


FIGURE 13. XRD analysis on annealed API 5L X65 day 5 specimens for 150 rpm ($V_{eq} = 0.4$ m/s, 0.3 Pa) and 250 rpm ($V_{eq} = 0.6$ m/s, 0.5 Pa) experiments.

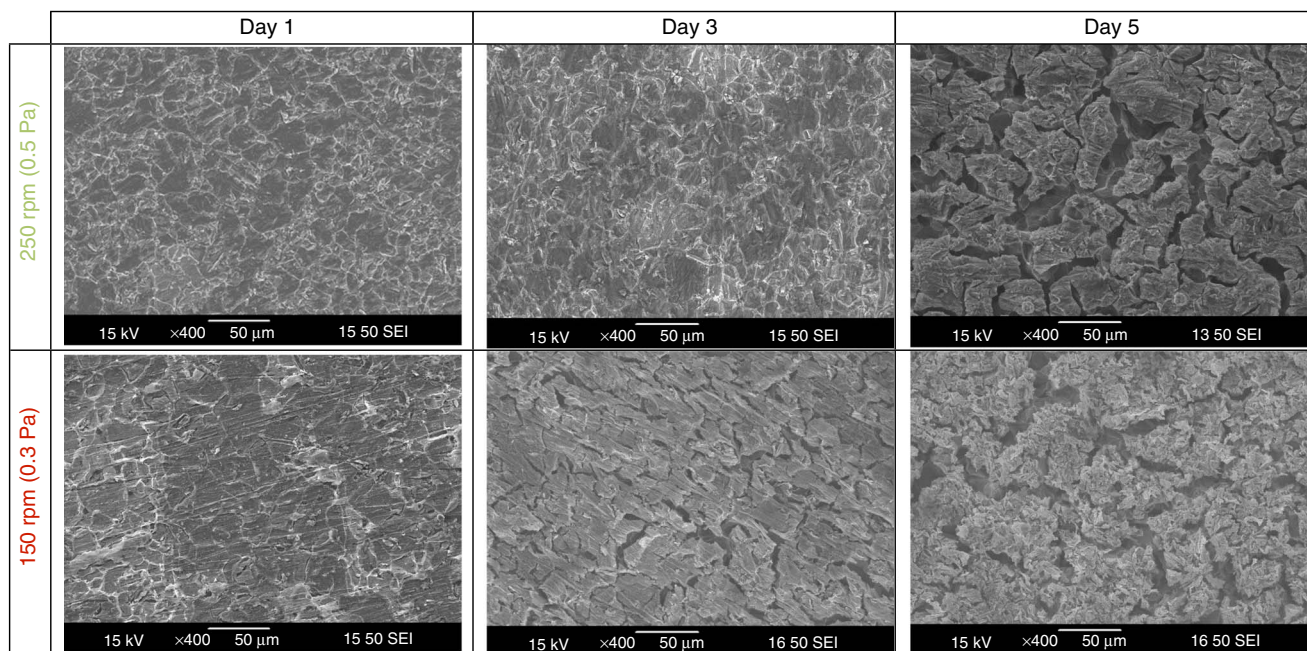


FIGURE 12. Comparison of surface morphologies over time for 150 rpm ($V_{eq} = 0.4$ m/s, 0.3 Pa) and 250 rpm ($V_{eq} = 0.6$ m/s, 0.5 Pa) experiments with annealed API 5L X65.

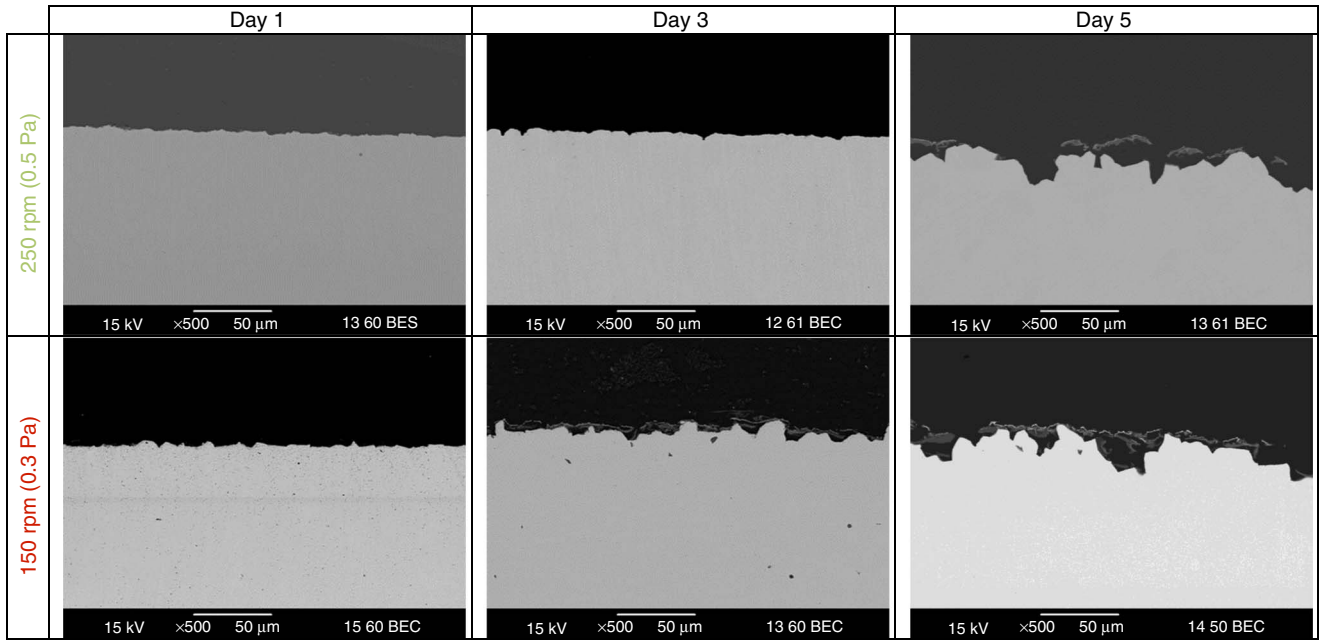


FIGURE 14. Comparison of cross-sectional morphologies over time for 150 rpm ($V_{eq} = 0.4$ m/s, 0.3 Pa) and 250 rpm ($V_{eq} = 0.6$ m/s, 0.5 Pa) experiments with annealed API 5L X65.

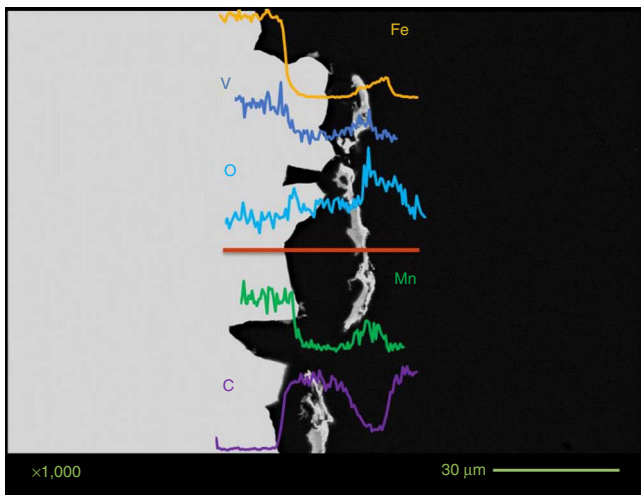


FIGURE 15. Cross-sectional morphology of annealed API 5L X65 for 250 rpm ($V_{eq} = 0.6$ m/s, 0.5 Pa) fifth day specimen showing elemental mapping.

which were less susceptible to removal by flow as a result of to the compactness and distribution of Fe_3C in a lamellar structure. In a tempered martensitic microstructure, as the distribution of Fe_3C was unordered and random in the material microstructure, the Fe_3C was more subjected to removal by flow (“flimsy” Fe_3C layer), which allowed for release of ferrous ions into the electrolyte without trapping them in the Fe_3C network, as opposed to what was found in a ferritic–pearlitic microstructure. Experiments were also performed with pure iron specimens,¹³ and results were similar to those in tempered martensitic specimens as no precipitation of $FeCO_3$ was observed on the specimen surface.

It was hypothesized that the material microstructure (Fe_3C) aids in the precipitation of $FeCO_3$ at high flow velocities. This hypothesis is partially true as only the ferritic–pearlitic microstructure combined with a high carbon content of 0.18 wt% C was able to precipitate $FeCO_3$ within a Fe_3C network. These findings seem to coincide with what other researchers suggest is a superior microstructure for $FeCO_3$ formation^{2,6} and is in opposition with others.¹ Table 4 compares findings for this set of experiments for all steels tested, including final LPR corrosion rates taken immediately prior to the last sample removal.

Table 4. Comparison of Equivalent Pipe Velocity, Wall Shear Stress, Final Corrosion Rate, and Precipitation of $FeCO_3$ for Each Experiment

Material	Equivalent Pipeline Velocities in 10 in pipe (m/s)		Wall Shear Stress (Pa)		Final LPR Corrosion Rate (mm/y)		WL Corrosion Rate (mm/y)		Did Precipitation of $FeCO_3$ Occur?
	150 rpm	250 rpm	150 rpm	250 rpm	150 rpm	250 rpm	150 rpm	250 rpm	
UNS G10180 ferritic–pearlitic	0.4	0.6	0.3	0.5	0.7	1.7	3	3.2	Yes
UNS G10180 tempered-martensitic					6.6	7.3	2.4	2.3	No
Annealed API 5L X65					2.8	3.0	1.8	2.0	No

CONCLUSIONS

Experiments with two rotational speeds and varying microstructures and carbon content were performed in an electrochemical three-electrode glass cell setup under controlled water-chemistry conditions. The results indicate the following:

- Retention of Fe₃C structures and nucleation of FeCO₃ were significantly reduced as turbulence/flow increased even when the bulk water chemistry was favorable to FeCO₃ precipitation.
- Material compositions with a higher carbon content, 0.18 wt% vs. 0.05 wt% C, favored precipitation of FeCO₃ because of their associated microstructure.
- Steel with a ferritic-pearlitic microstructure facilitated FeCO₃ precipitation as a result of the distribution/morphology of the Fe₃C structure, which enabled local water chemistry conditions near the metal surface to be favorable to precipitation of FeCO₃.

ACKNOWLEDGMENTS

Authors would like to thank sponsors of the Corrosion Center Joint Industry Project (CC JIP) at the Institute for Corrosion and Multiphase Technology (ICMT) for their financial support and the Center for Electrochemical Engineering Research for usage of analytical equipment, as well as Alexis Barxias for his assistance in the laboratory and Cody Shafer for equipment drawings. Ezechukwu Anyanwu is also acknowledged for flow simulations to determine shear stresses.

References

1. A. Dugstad, H. Hemmer, M. Seiersten, *Corrosion* 57, 4 (2001): p. 369.
2. N. Ochoa, C. Vega, N. Pébère, J. Lacaze, J.L. Brito, *Mater. Chem. Phys.* 156 (2015): p. 198.
3. F. Farel, B.N. Brown, S. Nešić, "Iron Carbide and its Influence on the Formation of Protective Iron Carbonate in CO₂ Corrosion of Mild Steel," CORROSION 2013, paper no. 2291 (Houston, TX: NACE International, 2013).
4. A. Groysman, *Corrosion for Everybody* (Houten, Netherlands: Springer Netherlands, 2010).
5. S. leamsupapong, B. Brown, M. Singer, S. Nešić, "Effect of Solution pH on Corrosion Product Layer Formation in a Controlled Water Chemistry System," CORROSION 2017, paper no. 9160 (Houston, TX: NACE, 2017).
6. F. F. Eliyan, A. Alfantazi, *Corros. Sci.* 85 (2014): p. 380.
7. T. Bernitsen, M. Seiersten, T. Hemmingsen, *Corrosion* 69, 6 (2013): p. 601.
8. R. Nyborg, "Initiation and Growth of Mesa Corrosion Attach During CO₂ Corrosion of Carbon Steel," CORROSION 98, paper no. 48 (Houston TX: NACE, 1998).
9. Y. Sun, "Localized CO₂ Corrosion in Horizontal Wet Gas Flow" (Ph.D. diss., Ohio University, 2003), p. 155.
10. ASTM G 31-72, "Standard Practice for Laboratory Immersion Corrosion Testing of Metals" (West Conshohocken, PA: ASTM International, 2004).
11. X. Zhong, B.N. Brown, W. Li, S. Nešić, M. Singer, "How to Maintain a Stable Solution Chemistry when Simulating CO₂ Corrosion in a Small Volume Laboratory System," CORROSION 2016, paper no. 7780 (Houston, TX: NACE, 2016).
12. S. leamsupapong, "Mechanisms of Iron Carbonate Formation on Mild Steel in Controlled Water Chemistry Conditions" (Ph.D. diss., Ohio University, 2016), p. 77-82.
13. M. Di Bonaventura, "Effect of Flow on the Formation of Iron Carbonate and Influence of Exposed Iron Carbide Layer" (Master's thesis, Ohio University, 2017), p. 112.
14. E. Anyanwu, "The Effect of Flow on the Development and Retention of Iron Sulfide Corrosion Product Layers" (Ph.D. diss., Ohio University, 2018), p. 65.
15. B.L. Bramfitt, A.O. Benschoter, *Metallographer's Guide: Practice and Procedures for Irons and Steels* (Materials Park, OH: ASM International, 2001), p. 37.
16. H. Chandler, *Heat Treater's Guide: Practices and Procedures for Irons and Steels*, 2nd ed. (Materials Park, OH: ASM International, 1995), p. 96-99, 139-141.
17. W.D. Callister, D.G. Rethwisch, *Materials Science and Engineering: An Introduction*, 9th ed. (New York, NY: Wiley, 2007), p. 665.
18. B.L. Bramfitt, *Structure/Property Relationships in Irons and Steels* (Materials Park, OH: ASM International, 1998), p. 34-38, 226-227.
19. R.D. Griffin, J.A. Griffin, G.M. Janowski, C.B. Moss, C.E. Bates, "The Effect of Quench Rate and Tempering Temperature on the Microstructure and Hardness of Commercial Steels," 18th ASM Heat Treating Society Conference and Exposition (Chicago, IL: ASM International, 1998), p. 320-328.
20. D. Dwivedi, K. Lepkova, T. Becker, *RSC Adv.* 7, 8 (2017): p. 4580.
21. Y. Yang, B.N. Brown, S. Nešić, "Mechanical Strength and Removal of a Protective Iron Carbonate Layer Formed on Mild Steel in CO₂ Corrosion," CORROSION 2010, paper no. 10383 (Houston, TX: NACE, 2010).
22. E. Akeer, "Effect of Carbon Steel Composition and Microstructure on CO₂ Corrosion?" (Ph.D. diss., Ohio University, 2014), p. 61.
23. R.W. Revie, H.H. Uhlig, *Uhlig's Corrosion Handbook*, 3rd ed. (Hoboken, NJ: John Wiley & Sons, 2011), p. 236.
24. M. Stern, A.L. Geary, *J. Electrochem. Soc.* 104, 1 (1957): p. 56.
25. D.N. Staicopolus, *J. Electrochem. Soc.* 110, 11 (1963): p. 1121.
26. F. Pessu, R. Barker, A. Neville, *Corrosion* 71, 12 (2015): p. 1452.
27. M. Singer, B.N. Brown, A. Camacho, S. Nestic, *Corrosion* 67, 1 (2011): p. 15004.
28. M. Singer, A. Camacho, B.N. Brown, S. Nešić, *Corrosion* 67, 8 (2011): p. 085003.
29. M. Singer, D. Hinkson, Z. Zhang, H. Wang, S. Nešić, *Corrosion* 69, 7 (2013): p. 719.
30. J.R. Vera, A. Vilorio, M. Castillo, A. Ikeda, M. Ueda, *European Federation of Corrosion* 13 (1995): p. 59.
31. A. Ikeda, M. Ueda, S. Mukai, "CO₂ Corrosion Behavior of Carbon Steel and Alloy Steel," CORROSION 1983, paper no. 45 (Houston, TX: NACE, 1983).
32. S. Al-Hassan, B. Mishra, D.L. Olson, M.M. Salama, *Corrosion* 54, 6 (1998): p. 480.
33. D. Clover, B. Kinsella, B. Pejčić, R. De Marco, *J. Appl. Electrochem.* 35, 2 (2005): p. 139.